Lateral Quantum-Confined Stark Effect for Integrated Quantum Dot Electroabsorption Modulators

Tommy Murphy, Christopher A. Broderick, Frank H. Peters, and Eoin P. O'Reilly

***Abstract*—Advances in III-V on Si quantum dot (QD) growth have enabled monolithic integration of high-performance electrically-pumped lasers on Si, as an enabling component for Si photonics. Another critical component is the electroabsorption modulator (EAM), which exploits the quantum-confined Stark effect (QCSE) to achieve high-speed modulation of laser signals. Conventional quantum well (QW) EAMs exploit a "vertical" QCSE via top and bottom electrical contacts. Rapid advancements in planar photonic integrated circuit technology motivate development of laterally-contacted EAMs, which offer benefits including reduced parasitic capacitance. The QCSE cannot be achieved via a lateral field in a QW, but can in a QD due to the three-dimensional carrier confinement. Here, theoretical analysis of the lateral-field QCSE in 1.3 μm In$_x$Ga$_{1-x}$As/GaAs QDs is undertaken. Comparing the QCSE produced by vertical and lateral electric fields for realistic QD morphology a robust lateral-field QCSE is demonstrated, with the optical absorption edge redshifting more rapidly vs. field strength than in a conventional QW-EAM. It is shown that lateral-field QD-EAM performance is expected to be strongly sensitive to the spectral linewidth of the band edge absorption, and can also depend upon the in-plane orientation of the lateral electric field. The impact of QD morphology – the base shape, aspect ratio and composition profile – is also quantified. It is demonstrated that In$_x$Ga$_{1-x}$As/GaAs QDs possessing high aspect ratios and low absorption linewidths are well-suited to develop lateral-field QD-EAMs. This suggests leveraging III-V on Si epitaxy to integrate EAMs with lasers or single-photon sources to realize high-speed Si photonic integrated circuits for applications in datacomms and linear optical quantum computing.**

***Index Terms*—Quantum dots, quantum-confined Stark effect (QCSE), electroabsorption modulators (EAMs), integrated photonics, silicon photonics.**

I. Introduction

ELECTROABSORPTION modulators (EAMs) enable high-speed modulation of optical signals by exploiting the quantum-confined Stark effect (QCSE) to redshift the optical absorption edge to a target modulation wavelength [1]. Early experiments on bulk semiconductors exploited the Franz-Keldysh effect [2], where the applied electric field contributes primarily to enhancing the spectral linewidth of the absorption edge, but produces minimal redshift [3]. The QCSE – the analog of the Franz-Keldysh effect in a quantum-confined heterostructure – produces a much stronger absorption edge redshift, allowing robust tuning of the absorption edge wavelength to achieve high-speed optical modulation [4]. EAMs based on quantum wells (QWs) have developed into staple components of InP-based integrated photonics, and are widely deployed in optical communications at datacom and telecom wavelengths [5].

The ongoing exponential growth in data consumption, and associated proliferation of datacoms infrastructure, mandate continuous improvements in the performance of high-bandwidth optical communications systems. Here, Si photonics has a key role to play, but remains intrinsically limited as a technological platform due to an absence of Si-compatible direct-gap semiconductors from which to realize electrically-pumped laser sources [6]. To overcome this challenge, significant research effort has been dedicated to the monolithic integration of III-V quantum dots (QDs) on Si [7], [8], [9], [10], [11]. Systematic refinement of III-V on Si epitaxy has underpinned impressive progress [6], [12], [13], [14], [15], with 1.3 μm In$_x$Ga$_{1-x}$As on Si QD lasers now demonstrating high performance [16], [17], [18], [19]. Combined with the potential to develop hybrid quantum photonic circuits enabling linear optical quantum computing applications through the integration of III-V QD single-photon sources [20], this constitutes a strong imperative to exploit III-V QDs to deliver enhanced functionality for Si photonics. Despite their importance for QD integrated photonics, little research attention has yet been dedicated to the development of EAMs that exploit a QD active region [12]. The planar architecture of photonic integrated circuits suggests exploration of "lateral" EAMs defined by planar electrical contacts, as opposed to the top and bottom contacts of conventional "vertical" QW-EAMs. Lateral EAMs have been considered in QWs, motivated by the potential of lateral contacting to reduce parasitic capacitance [21]. However, the lack of carrier confinement perpendicular to the growth direction in a QW means that a lateral electric field generates only a weak (Franz-Keldysh-like) redshift of the absorption edge.

In this Article we present a proof-of-principle theoretical analysis that identifies the lateral-field QCSE in 1.3 μm In$_x$Ga$_{1-x}$As QDs as a viable route to realize high-speed datacom EAMs.

Received 13 January 2025; revised 10 March 2025; accepted 12 March 2025. Date of publication 17 March 2025; date of current version 21 April 2025. This work was supported in part by Taighde Éireann - Research Ireland via the Irish Photonic Integration Centre under Grant 12/RC/2276_P2, and in part by a Royal Society-Research Ireland University Research Fellowship under Grant URF/R1/231340, held by C.A.B. This work was supported in part by using computational resources provided by the Irish Centre for High-End Computing project TIPHY089C. *(Corresponding authors: Tommy Murphy; Christopher A. Broderick.)*

The authors are with Tyndall National Institute, University College Cork, Lee Maltings, Dyke Parade, T12 R5CP Cork, Ireland, and also with the School of Physics, University College Cork, T12 YN60 Cork, Ireland (e-mail: tommy.murphy@umail.ucc.ie; christopher.broderick@ucc.ie).

The data that support the findings of this study are openly available via the Zenodo repository at https://zenodo.org/records/14230795.

Color versions of one or more figures in this article are available at https://doi.org/10.1109/JSTQE.2025.3552024.

Digital Object Identifier 10.1109/JSTQE.2025.3552024

The three-dimensional carrier confinement in a QD allows the exploitation of the QCSE generated by a lateral electric field, offering the possibility to realize high-speed EAMs for on-chip integration with high-performance 1.3 μm lasers. This is demonstrated via QD electroabsorption analysis based on multi-band $\mathbf{k}{\cdot}\mathbf{p}$ calculations, including strain and piezoelectric effects (cf. Section II). The large base-to-height aspect ratio (AR) of self-assembled III-V QDs gives rise to a lateral QCSE that is significantly stronger than its previously explored vertical counterpart. We quantify the sensitivity of the lateral-field QCSE to the QD morphology and absorption edge linewidth. We also highlight an interplay between the applied electric field and the piezoelectric potential within the QD, which can generate an anisotropic lateral QCSE. Our systematic analysis identifies that QDs having ARs $\gtrsim$ 4:1 and absorption edge linewidths $\lesssim 25$ meV are expected to render lateral QD-EAM operation viable. Our results identify the potential to leverage existing III-V on Si QD epitaxy to realize high-speed EAMs that can be integrated on-chip with existing QD lasers.

II. Methods

Our QD electronic structure calculations employ an 8-band $\mathbf{k}\cdot\mathbf{p}$ Hamiltonian [22], [23]. Band offsets are determined in the absence of strain via the model solid theory, following which the impact of strain is incorporated via the Bir-Pikus Hamiltonian [22]. The strain fields, piezoelectric potential and electronic structure are calculated in reciprocal space using a semi-analytical plane wave expansion method (PWEM) [24], [25]. The strain field calculations follow the Green's function approach of Ref. [26], and the piezoelectric potential $\phi_{\text{pz}}(\mathbf{r})$ is computed by solving Poisson's equation analytically in reciprocal space for the charge density induced by the piezoelectric polarization [24]. Given the appreciable impact of second-order piezoelectricity in determining the energy ordering and spatial orientation of QD eigenstates [27], we include first- and second-order contributions to $\phi_{\text{pz}}(\mathbf{r})$. The applied electric field $\mathbf{F}$ is explicitly incorporated in the Hamiltonian via its electrostatic potential $\phi_{\text{ext}}(\mathbf{r}) = -e\,\mathbf{F}\cdot\mathbf{r}$. The elastic and band parameters employed in our calculations follow Ref. [28], while the piezoelectric coefficients are from Ref. [29].

The PWEM consists of expanding the QD eigenstate envelope functions as a Fourier series

$$|\psi_n(\mathbf{r})\rangle = \frac{1}{\sqrt{\Omega}} \sum_{b=1}^{8} \sum_{\{\mathbf{G}\}} a_{nb\mathbf{G}}\, e^{i\mathbf{G}\cdot\mathbf{r}}\, |u_b\rangle \,, \qquad (1)$$

where b indexes the Bloch basis states $|u_b\rangle$ of the underlying bulk 8-band $\mathbf{k}\cdot\mathbf{p}$ Hamiltonian, $\Omega = L_x L_y L_z$ is the volume of the calculational supercell, and $\{\mathbf{G}\}$ denotes the set of discrete reciprocal lattice vectors $\mathbf{G} = (2\pi m_x/L_x)\,\widehat{x} + (2\pi m_y/L_y)\,\widehat{y} + (2\pi m_z/L_z)\,\widehat{z}$ for integers m_j, where $|m_j| \leq M_j$ such that the basis set consists of $2M_j + 1$ plane waves along each Cartesian direction $j = x, y$ or z. This enables analytical evaluation of the QD Hamiltonian matrix in reciprocal space. The analytical calculation consists of (i) quantizing the elements $H_{bb'}(\mathbf{k})$ of the bulk Hamiltonian via $\mathbf{k} \to -i\nabla$, subject to symmetrization to impose continuity of probability current density, and (ii) generating the matrix representation of the resulting position-dependent operators $\widehat{H}_{bb'}(\mathbf{r})$ in the plane wave basis as [24], [25]

$$(\widehat{H}_{bb'})_{\mathbf{G}\mathbf{G}'} = \frac{1}{\Omega} \int_{\Omega} e^{-i\mathbf{G}\cdot\mathbf{r}}\, \widehat{H}_{bb'}(\mathbf{r})\, e^{i\mathbf{G}'\cdot\mathbf{r}}\, \mathbf{dr} \,. \qquad (2)$$

The QD morphology is described via the characteristic function $\chi(\mathbf{r})$, which is assigned a value of 1 (0) inside (outside) the QD. In the PWEM, geometric information is encapsulated by the Fourier transform $\widetilde{\chi}(\mathbf{G})$ of $\chi(\mathbf{r})$ [24]. If $\widetilde{\chi}(\mathbf{G})$ can be computed analytically [26], it then follows that Eq. (2) can be evaluated analytically. This allows the QD Hamiltonian to be determined without recourse to finite difference or element approximations to real-space derivatives. Once the Hamiltonian matrix has been set up in this manner, the QD eigenstates are then computed via exact diagonalization. We employ $L_x = L_y \approx 60$ nm and $L_z \approx 35$ nm, with minor adjustments depending on QD AR. Plane wave basis sets having $M_x = M_y = 7$ and $M_z = 10$ were found to be sufficient to converge the bound QD eigenstates.

The strain fields $\epsilon_{ij}(\mathbf{r})$ can exhibit large decay lengths around embedded QDs. We therefore calculate the strain field Fourier transforms $\widetilde{\epsilon}_{ij}(\mathbf{G})$ in a large supercell of volume Ω_{str}. These $\widetilde{\epsilon}_{ij}(\mathbf{G})$ are downsampled into the supercell of volume $\Omega < \Omega_{\text{str}}$ employed in the electronic structure calculations [30]. This removes artifacts generated by the PWEM's periodic boundary conditions from the strain calculation, allowing the incorporation of realistic strain fields without incurring the computational cost associated with large-Ω electronic structure calculations.

Using the calculated QD eigenstates we compute the optical absorption spectrum via Fermi's golden rule as [1]

$$\alpha(\hbar\omega) = \frac{\pi^2}{\epsilon_0 n_r m_0^2 \omega \Omega} \sum_{n_c, n_v} |\widehat{e}\cdot\mathbf{p}_{n_c,n_v}|^2\, \delta(E_{n_c} - E_{n_v} - \hbar\omega)\,, \qquad (3)$$

where n_c and n_v index the electron and hole states, having respective energies E_{n_c} and E_{n_v}, $\hbar\omega$ is the photon energy, and n_r is the refractive index. We replace the Dirac delta distribution by a Gaussian lineshape. The magnitude of the optical absorption is governed by the momentum matrix elements $\widehat{e}\cdot\mathbf{p}_{n_c,n_v}$, which we evaluate via the Hellmann-Feynman theorem [31] using the PWEM Hamiltonian and eigenstates [32]

$$\widehat{e}\cdot\mathbf{p}_{n_c,n_v} = \frac{m_0}{\hbar} \langle \psi_{n_c}(\mathbf{r}) | \widehat{e}\cdot\nabla_{\mathbf{k}}\widehat{H} | \psi_{n_v}(\mathbf{r}) \rangle \,, \qquad (4)$$

where $\widehat{e}\cdot\nabla_{\mathbf{k}}\widehat{H}$ is the directional derivative of the QD Hamiltonian $\widehat{H}$ with respect to wave vector $\mathbf{k}$, along the direction specified by the photon polarization $\widehat{e}$.

III. Results

Investigation of the lateral-field QCSE requires defining a realistic QD morphology. It is widely accepted that [001]-oriented $In_xGa_{1-x}As$/GaAs QDs assume a truncated pyramidal or lens shape [27], [33], [34], [35], in which the QD height h is small relative to the base length d, with typical ARs d:h being $\gtrsim$ 3:1 [34], [35]. Two primary considerations inform our choice of QDs. First, even in a highly symmetric QD shape – e.g. a circular-base lens or truncated cone ($C_{\infty v}$) – the piezoelectric potential $\phi_{\text{pz}}(\mathbf{r})$

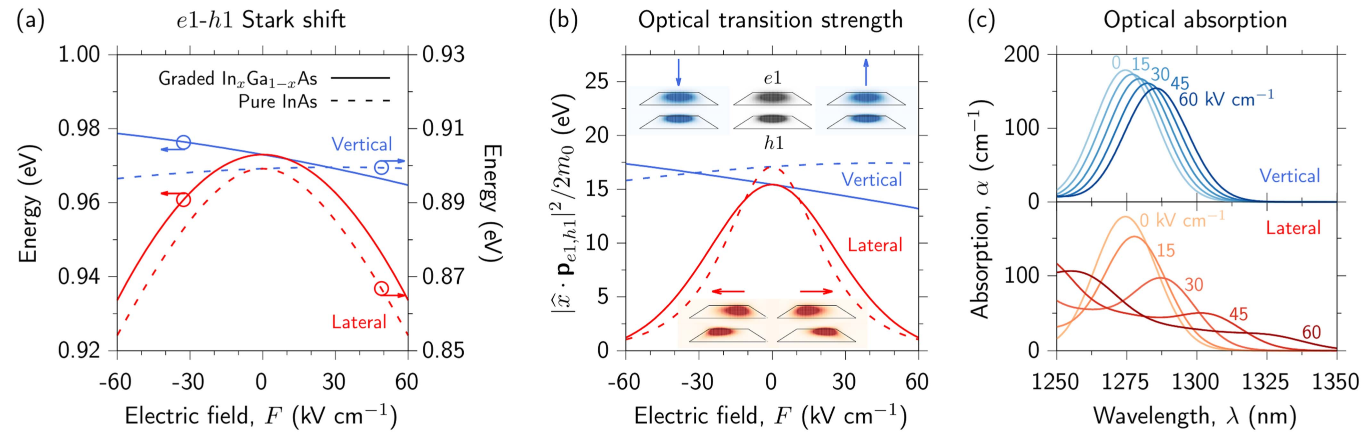

Fig. 1. (a) Stark shift of the $e1$-$h1$ QD band gap under vertical $\mathbf{F} = F\widehat{z} \parallel$ [001] (blue) and lateral $\mathbf{F} = F\widehat{x} \parallel$ [100] (red) applied electric fields, for the composition-graded $In_xGa_{1-x}As$ QD described in the text (solid lines) and a pure InAs QD (dashed lines). The left- and right-hand ordinates respectively refer to the $e1$-$h1$ band gap of the composition-graded and pure QDs. (b) Kane energy (optical transition strength) vs. vertical [001] (blue) and lateral [100] (red) applied electric field strength, for the $e1$-$h1$ optical transition of the QDs of (a). Insets show the corresponding $e1$ (upper) and $h1$ (lower) probability densities at applied electric field strength $F = 30$ kV cm^{-1}, where arrows denote the direction of the applied field. (c) Optical absorption spectra for applied vertical (upper) and lateral (lower) electric fields of strength $F = 0$, 15, 30, 45 and 60 kV cm^{-1}, for the composition-graded QD of (a) and (b). The optical transition strengths in (b), and optical absorption spectra in (c), are for photon polarization $\widehat{e} = \widehat{x}$.

imposes the lower C_{2v} symmetry of the zinc blende lattice. Previous calculations indicate that this impacts the orientation of the electron and hole wave functions in the QD plane [27], and thus impacts the electron-hole spatial overlaps that determine the optical (momentum) matrix elements. Second, spectroscopic measurements vs. vertical applied electric field for $In_xGa_{1-x}As$/GaAs QDs have revealed "inverted" electron-hole alignment, in which the ground state hole $h1$ is localized above the ground state electron $e1$ along [001] [36]. This alignment is "inverted" since it runs counter to theoretical predictions for pure InAs/GaAs QDs, in which the asymmetric QD shape along [001] causes $e1$ to localize above $h1$. Subsequent analysis showed that inverted $e1$-$h1$ alignment is consistent with an In composition gradient along [001] [37]. A vertical composition gradient of this type can arise in a QD due to In diffusion during growth and can be modeled by considering that a nominally pure InAs QD is alloyed $In_xGa_{1-x}As$ at its base, with the In composition x increasing to give pure InAs at the apex. This morphology has a marked impact on the conventional vertical QCSE [36], [37]. We therefore analyze $In_xGa_{1-x}As$/GaAs QDs that: (i) are truncated pyramids or truncated cones, the respective square and circular lateral shapes of which represent the two extremes relevant to real QDs [27], and (ii) are $In_xGa_{1-x}As$ alloys having $x < 1$ at the base, with x increasing linearly to $x = 1$ at the apex [37].

Using this realistic QD morphology, we begin by comparing the vertical- and lateral-field QCSE in exemplar QDs that are pure InAs or possess an In composition gradient along [001]. Following this we analyze the lateral-field electroabsorption, highlighting the expected sensitivity of lateral QD-EAM operation to the linewidth of the band edge optical absorption. We then turn our attention to the impact of the lateral field orientation and highlight an interplay between $\phi_{\text{pz}}(\mathbf{r})$ and the electrostatic potential $\phi_{\text{ext}}(\mathbf{r})$ generated by the applied electric field, which can produce an anisotropic QCSE response. Finally, we consider the impact of the QD morphology by quantifying the dependence of the lateral-field QCSE on the AR and vertical In composition profile.

A. Vertical- Vs. lateral-Field QCSE

Our prototype 1.3 μm QD is a square-based, 50% truncated pyramid with base edges parallel to [100] and [010], base side length $d = 31$ nm and height $h = 6.2$ nm along [001] (AR = 5:1). The QD has composition $In_{0.5}Ga_{0.5}As$ ($x = 0.5$) at its base, which increases linearly along [001] to pure InAs ($x = 1$) at the apex. We employ Cartesian coordinates in which the unit vectors $\widehat{x}$, $\widehat{y}$ and $\widehat{z}$ are respectively aligned with the [100], [010] and [001] principal cubic crystal axes. To examine the importance of modeling the QD to have a vertical In composition gradient, in Fig. 1(a) and (b) we compare the QCSE response to a vertical field $\mathbf{F} = F\widehat{z} \parallel$ [001] (blue) and a lateral field $\mathbf{F} = F\widehat{x} \parallel$ [100] (red), for the prototypical composition-graded QD (solid lines) and a pure InAs QD of equal shape and size (dashed lines).

Beginning in Fig. 1(a) with the Stark shift of the $e1$-$h1$ QD band gap, we note the marked impact of the In composition gradient in the vertical-field case. In the pure InAs QD the band gap increases with increasing F, with this trend reversed in the composition-graded QD. The maximum of the vertical-field band gap vs. F curve lies out of scale to the right (left) for the pure InAs (composition-graded) QD. The composition-graded QD reproduces the observed experimental trend in the vertical-field case [36], confirming that a vertical In composition gradient captures the inverted electron-hole alignment along [001] [37]. Turning our attention to the lateral-field Stark shift, we note two key differences vs. the vertical-field case: (i) the magnitude of the Stark shift is significantly larger for the lateral field, and (ii) the dependence of the band gap on the lateral field strength is independent of $\mathbf{F}$ being applied parallel or anti-parallel to [100]. Indeed, due to the lateral symmetry of the QD we note that the lateral-field QCSE is insensitive to $\mathbf{F}$ being applied along either [100] or [010]. This, however, is not the case for arbitrary in-plane orientation of $\mathbf{F}$. The interplay between $\phi_{\text{pz}}(\mathbf{r})$ and $\phi_{\text{ext}}(\mathbf{r})$ can produce anisotropy in the QCSE when $\mathbf{F}$ is not applied along either [100] or [010] (cf. Section III-C). We note that the Stark shift in the lateral-field case is qualitatively identical, and quantitatively similar, for the pure InAs and composition-graded QDs. While this suggests that an In composition gradient along [001] has minimal impact on the lateral-field QCSE, it can have a pronounced impact at lower AR (cf. Section III-D).

The larger magnitude of the lateral-field Stark shift can be readily ascertained based on the standard perturbation theoretic treatment of the QCSE for a particle-in-a-box [1]. The Stark shift is given to leading order by $\Delta E(F) \propto -m^* a^4 F^2$ for an electron of effective mass m^* in a QW of thickness a. We can then roughly estimate that the ratio of the lateral- to vertical-field Stark shift scales $\propto (d/h)^4$ at field strength F. While this simple QW analysis neglects several factors – e.g. the QD morphology and anisotropy of m^* – it overestimates but is consistent with the lateral-field Stark shift strongly exceeding its vertical-field counterpart at fixed F when $d/h > 1$. This is expected to hold generally for self-assembled III-V QDs, which possess ARs $\gtrsim$ 3:1 (cf. Section III-D).

Fig. 1(b) shows the dependence of the $e1$-$h1$ optical transition strength vs. F, presented as the Kane energy $|\widehat{x} \cdot \mathbf{p}_{e1,h1}|^2/2m_0$. As will be the case throughout, the photon polarization has been set parallel to the lateral applied electric field: here, $\widehat{e} = \widehat{x} \parallel$ [100]. Insets show the $e1$ and $h1$ probability densities $|\psi_{e1}(\mathbf{r})|^2$ and $|\psi_{h1}(\mathbf{r})|^2$ at zero field (top-center; grey), at vertical applied fields $F = \pm 30$ kV cm^{-1} (top-left and top-right; blue) and at lateral applied fields $F = \pm 30$ kV cm^{-1} (bottom-left and bottom-right; red), where arrows denote the direction of the applied field. Applying a vertical field $F > 0$ acts to push $e1$ downwards ($h1$ upwards) along [001]. In the pure InAs QD, where $e1$ is localized above $h1$, this acts to increase the $e1$-$h1$ spatial overlap $|\langle\psi_{e1}(\mathbf{r})|\psi_{h1}(\mathbf{r})\rangle|^2$, thereby increasing $|\widehat{x} \cdot \mathbf{p}_{e1,h1}|^2$. This trend is reversed in the composition-graded QD due to the inverted $e1$-$h1$ alignment: applying a vertical field $F > 0$ reduces the $e1$-$h1$ spatial overlap by pushing $e1$ ($h1$) further towards the base (apex) of the QD, reducing the optical transition strength with increasing F. As such, the inverted $e1$-$h1$ alignment in the composition-graded QD again reverses the trend calculated for the pure InAs QD.

Since $e1$ and $h1$ are not laterally offset at zero field, the largest $e1$-$h1$ spatial overlap in the lateral-field case occurs at $F = 0$. The maximum of the lateral-field band gap vs. F thus resides at $F = 0$, and the Stark shift varies roughly $\propto -F^2$. This contrasts with the vertical-field case in which the Stark shift varies closer to $\propto -F$ about $F = 0$, due to the maximum band gap being offset to large $|\mathbf{F}|$. Due to the large AR, carriers experience less spatial confinement perpendicular to [001]. Application of a lateral field shifts $e1$ and $h1$ in opposite directions in the plane of the QD, providing significantly larger spatial extent within which to redistribute $|\psi_{e1}(\mathbf{r})|^2$ and $|\psi_{h1}(\mathbf{r})|^2$. This results in a more rapid decrease of the optical transition strength in the lateral-field case. Taken together, Fig. 1(a) and (b) suggest that the lateral confinement provided by a QD heterostructure, combined with the large ARs exhibited by self-assembled QDs, leads to a robust lateral-field QCSE.

B. Lateral-Field Electroabsorption

Fig. 1(c) shows the optical absorption spectra of the composition-graded QD of Fig. 1(a) and (b) for vertical (upper panel) and lateral (lower panel) applied fields. The Gaussian full width at half maximum (FWHM) $\Delta = 20$ meV employed in absorption calculations (cf. Section II) is chosen at the lower end of experimental reports [38], [39]. The QCSE is evident in both cases and the trends of Fig. 1(a) and (b) are borne out: a lateral field produces a more pronounced QCSE at fixed F. For lateral fields $F = 30 - 45$ kV cm^{-1} the absorption edge can be tuned close to 1.3 μm, confirming the potential to develop lateral-field QD-EAMs for III-V on Si datacoms.

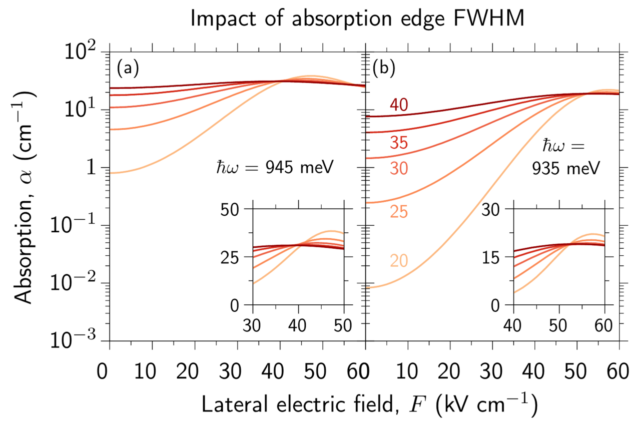

Fig. 2. Optical absorption α vs. lateral electric field strength F at photon energies (a) $\hbar\omega = 945$ meV ($\lambda = 1.31$ μm), and (b) $\hbar\omega = 935$ meV ($\lambda = 1.33$ μm), calculated for the composition-graded QD of Fig. 1 with Gaussian FWHM $\Delta = 20 - 40$ meV (darkening red). Insets show α vs. F on a linear scale, close to the peak absorption.

In the lateral-field case, at a modulation wavelength $\lambda =$ 1.31 μm ($\hbar\omega = 945$ meV) the calculated zero-field absorption is $\alpha_0 = 0.8$ cm^{-1}, which increases to $\alpha_F = 37.5$ cm^{-1} at $F =$ 45 kVcm^{-1}. This constitutes an enhancement $\alpha_F/\alpha_0 = 47$, an important figure of merit to quantify EAM performance [40], [41]. While this high α_F/α_0 at the chosen modulation wavelength suggests viable EAM operation, we note that the calculated below-gap α_0, and hence α_F/α_0, is strongly sensitive to the choice of Gaussian FWHM. While the absorption peak in a QD sample may not be exactly Gaussian, it is nevertheless worth to consider how the Gaussian FWHM influences the maximum value of α_F/α_0 that can be expected for a given shift in absorption edge wavelength. Consider a Gaussian with peak and standard deviation energies E_0 and σ, such that $\alpha_0(\hbar\omega) \propto \exp(-(\hbar\omega - E_0)^2/2\sigma^2)$ with FWHM $\Delta = 2\sqrt{2\ln 2}\,\sigma$. As $\hbar\omega$ moves away from E_0, $\alpha_0(\hbar\omega)$ decreases by a factor of N when $\hbar\omega - E_0 = \sqrt{2\ln N}\,\sigma = \sqrt{\log_2 N}\,\Delta/2$. The change in $\hbar\omega$ required to reduce the zero-field absorption $\alpha_0(\hbar\omega)$ by a factor of N is thus $\propto \Delta$. Making the simplifying assumption that the peak absorption is independent of F, the absorption peak must therefore redshift by at least $0.91\,\Delta$ to achieve $\alpha_F/\alpha_0 = 10$, and by at least $1.29\,\Delta$ for $\alpha_F/\alpha_0 = 100$.

It is therefore of practical importance to quantify how the absorption edge FWHM can impact expected QD-EAM performance. Approaches to grow highly uniform QDs have produced samples with low FWHM $<$ 17 meV [38], [39]. More typical FWHM values can be ascertained by examining those measured during QD laser operation, where typical FWHMs $\sim$ 30 meV have been reported [8], [17], [19], [42], with slightly lower values achievable when out-diffusion of In from the QD is suppressed (e.g. FWHM $=$ 24 meV in Ref. [43]). Fig. 2

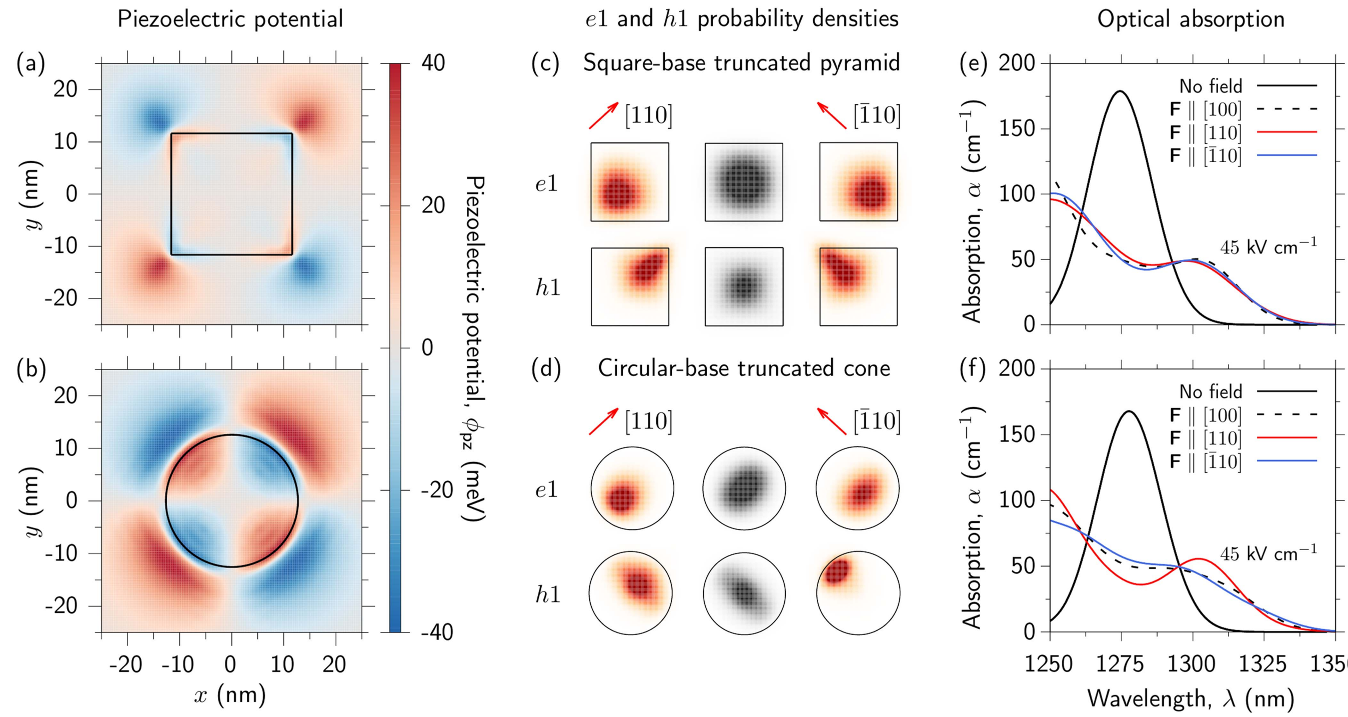

Fig. 3. Left: Cross-sectional view of the piezoelectric potential $\phi_{\text{pz}}(\mathbf{r})$ for the (a) square-base truncated pyramid, and (b) circular-base truncated cone QDs described in the text. Centre: Cross-sectional views of the ground state electron ($e1$) and hole ($h1$) probability densities for the (c) square-base truncated pyramid, and (d) circular-base truncated cone QDs of (a) and (b), respectively. Probability densities are shown at zero-field (center, gray) and for lateral applied fields having $F = 30$ kV cm^{-1} and oriented along [110] (left, red) and [$\bar{1}$10] (right, red). Cross-sections in (a) – (d) are shown in the (001) plane, at one-half of the QD height h along [001]. Right: Optical absorption spectra for the (e) square-base truncated pyramid, and (f) circular-base truncated cone QDs of (a) and (b), respectively. Absorption spectra are shown at zero field (solid black) and for lateral electric fields having $F = 45$ kV cm^{-1} and oriented along [100] (dashed black), [110] (solid red) and [$\bar{1}$10] (solid blue).

summarizes the dependence of α_F vs. lateral F on FWHM at fixed photon energies (a) $\hbar\omega = 945$ and (b) $\hbar\omega = 935$ meV, for the composition-graded QD of Fig. 1. The exponential dependence of the below-gap absorption tail on FWHM causes α_0 to vary by several orders of magnitude in response to minor changes in FWHM. For example, with $\hbar\omega = 945$ meV and $F = 45$ kV cm^{-1} as above, reducing Δ to 15 meV increases α_F/α_0 to 2,650, while increasing Δ to 25 meV decreases α_F/α_0 to 7.6. The requirement for low absorption edge FWHM to achieve viable α_F/α_0 thus appears stringent, but can be mitigated by blueshifting the zero-field QD band gap further from the desired modulation wavelength. Pushing the zero-field absorption edge to shorter wavelength reduces α_0 at the modulation wavelength, allowing to recover α_F/α_0. This is confirmed in Fig. 2(b), where such a blueshift has been emulated by redshifting the modulation wavelength away from the zero-field QD band gap of 973 meV for our prototypical QD; cf. Fig. 1(a), from 945 to 935 meV. We find that this increases the FWHM range for viable EAM operation. For $\Delta = 25$ meV and $\hbar\omega = 935$ meV we find $\alpha_0 = 0.25$ cm^{-1} and $\alpha_F = 20.2$ cm^{-1} at $F = 57$ kV cm^{-1} (the field strength at which α_F is maximized, cf. Fig. 2(b)), resulting in $\alpha_F/\alpha_0 = 81$ having increased by an order of magnitude vs. $\alpha_F/\alpha_0 = 7.6$ at $\hbar\omega = 945$ meV. However, this recovery in α_F/α_0 is achieved at the expense of lower overall absorption, as a consequence of requiring larger F to redshift the absorption edge 10 meV further from the zero-field band gap. Nonetheless, this demonstrates that while lateral-field QD-EAM performance is expected to be optimized in structures displaying low FWHM, operation should be viable in structures displaying larger FWHM provided the QDs possess slightly larger zero-field band gap relative to the modulation wavelength.

C. Lateral Field Orientation

Generally, it can be expected that the lateral QCSE response depends on the in-plane orientation of $\mathbf{F}$, due to the interplay of $\phi_{\text{pz}}(\mathbf{r})$ and $\phi_{\text{ext}}(\mathbf{r})$. Since the waveguide and electrical contacts can run along different directions in a photonic integrated circuit, it is important to quantify anisotropy in the lateral-field QCSE response. A QD may be elongated along a specific lateral direction, with dependence on growth conditions meaning that QD morphology can vary not only between samples but also depending on the position of a given QD within a sample. Transmission electron microscopy typically images QDs perpendicular to the growth direction, and thus fails to elucidate the in-plane morphology. Previous theory has employed rectilinear and round QD cross-sections: we consider both, to quantify the impact of QD base shape on the lateral QCSE. To capture these two extremes, we analyze the dependence of the QCSE on lateral field orientation in square-base (truncated pyramid) and circular-base (truncated cone) QDs. The square base represents

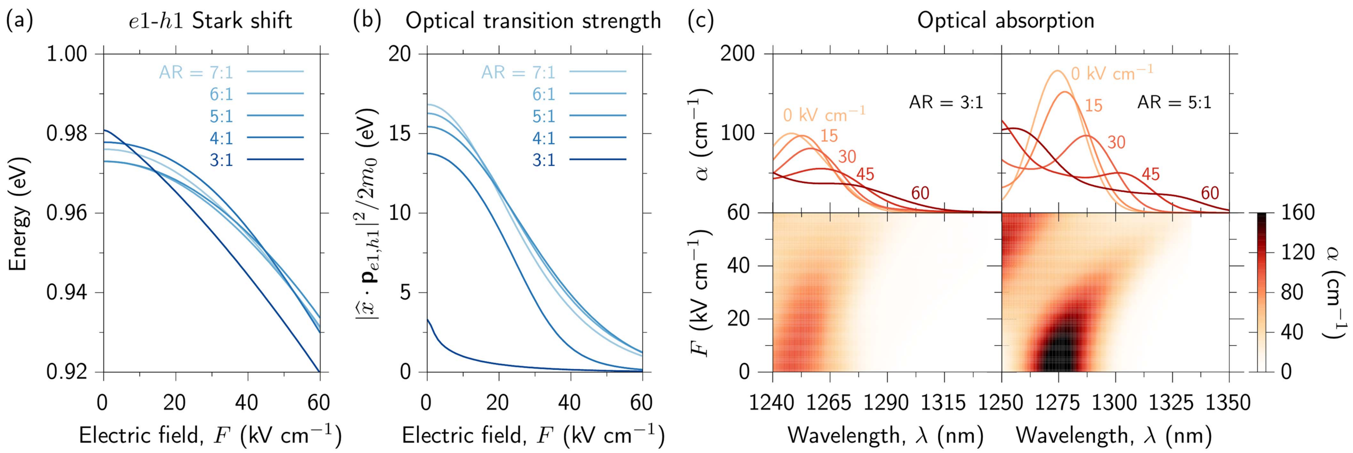

Fig. 4. (a) Stark shift, and (b) Kane energy (optical transition strength) of the $e1$-$h1$ band gap vs. [100] lateral applied electric field strength F for square-base truncated pyramidal QDs having AR = 7:1 to 3:1 (darkening blue). (c) Absorption spectra for the QDs of (a) and (b) having AR = 3:1 (left) and 5:1 (right). Upper panels show the absorption spectra for electric field strengths $F = 0 - 60$ kV cm^{-1} (darkening red). For each QD the lower panel highlights the evolution of the band edge electroabsorption.

the idealized case in which the QD facets are strictly delineated by crystallographic planes. The truncated pyramid dimensions are as above (cf. Section III-A), while the truncated cone has the same AR ($= 5{:}1$) with base diameter $d = 33.6$ nm and height $h = 6.72$ nm. The truncated pyramid presents a different AR when $\mathbf{F}$ is applied along the [100] or [010] base sides ($= d/h$) vs. along the [110] or [$\bar{1}$10] directions at 45° to the base sides ($= \sqrt{2}\, d/h$).

Fig. 3(a) and (b) respectively show cross sections of $\phi_{\text{pz}}(\mathbf{r})$ in the (001) plane for the truncated pyramid and cone QDs. Corresponding $e1$ and $h1$ probability densities are shown in Fig. 3(c) and (d), where the center columns show the zero-field probability densities, and the left and right columns respectively show the probability densities for $F = 30$ kV cm^{-1} applied along [110] and [$\bar{1}$10]. $\phi_{\text{pz}}(\mathbf{r})$ acts to orient the zero-field $e1$ ($h1$) probability density along [110] ([$\bar{1}$10]). The extent to which this orientation occurs depends closely on the QD base shape: it is minimal in the square-base QD due to $\phi_{\text{pz}}(\mathbf{r})$ being near-zero within the QD, but is pronounced in the circular-base QD due to $\phi_{\text{pz}}(\mathbf{r})$ creating low (high) energy potential pockets for electrons (holes) along [110] ([$\bar{1}$10]). This in-plane wave function orientation impacts the absorption via the spatial overlaps that determine the optical transition strengths, leading to a different QCSE response for $\mathbf{F} \parallel$ [100], [110] or [$\bar{1}$10].

Fig. 3(e) and (f) respectively show the absorption spectra of the square- and circular-base QDs, at zero field (solid black) and for $F = 45$ kV cm^{-1} along [100] (dashed black), [110] (red) and [$\bar{1}$10] (blue). At zero field we note slightly lower peak absorption in the circular-base QD, as a consequence of the wave function orientation reducing the $e1$-$h1$ overlap vs. that in the square-base QD. For the square-base QD the Stark shift and band edge absorption are impacted to a small degree by the lateral field orientation – e.g. the absorption at $\hbar\omega = 945$ meV for $\mathbf{F} \parallel$ [110] is 89% of that for $\mathbf{F} \parallel$ [100]. This is a consequence of the effective AR along [110] being $\sqrt{2}$ times larger than along [100], providing more distance within the QD for $e1$ and $h1$ to separate when $\mathbf{F} \parallel$ [110]. $\phi_{\text{pz}}(\mathbf{r})$ is not sufficiently large within the square-base QD to meaningfully distinguish the [110] and [$\bar{1}$10] directions, leading to minimal difference ($\lesssim 5\%$) in absorption at $F = 45$ kV cm^{-1}. The larger $\phi_{\text{pz}}(\mathbf{r})$ in the circular-base QD leads to more pronounced anisotropy in the lateral QCSE, with $\mathbf{F} \parallel$ [110] producing larger absorption at 945 meV vs. applying $\mathbf{F} \parallel$ [100] or [$\bar{1}$10]. This is a direct consequence of the impact of $\phi_{\text{pz}}(\mathbf{r})$ on the $e1$-$h1$ overlap under an applied field: Fig. 3(d) confirms that applying $\mathbf{F} \parallel$ [110] limits $h1$ from reaching the QD facet due to having $\phi_{\text{pz}}(\mathbf{r}) < 0$ inside the QD along that direction. This acts to preserve larger $e1$-$h1$ overlap vs. $\mathbf{F}$ being applied in a direction other than [110]. For example, for $\mathbf{F} \parallel$ [100] ([$\bar{1}$10]) we find at $F = 45$ kV cm^{-1} that the absorption at 945 meV is reduced by 18% (28%) compared to that for $\mathbf{F} \parallel$ [110].

D. QD Morphology

Having focused so far on QDs having fixed AR = 5:1, we turn our attention to the impact of the QD morphology on the lateral QCSE in 50% truncated pyramidal QDs with $\mathbf{F} \parallel$ [100]. As we vary AR = $d{:}h$, we adjust d and h to retain a zero-field $e1$-$h1$ band gap close to 980 meV (1.27 μm) while keeping the total amount of InAs in the QD fixed. This yields $d = 26.1$ nm for an AR of 3:1, increasing to 34.7 nm as the AR is increased to 7:1. Fig. 4(a) and (b) show the $e1$-$h1$ Stark shift and optical transition strength vs. F for ARs ranging from 7:1 to 3:1 (darkening blue). The Stark shifts are $\propto -F^2$ at higher AR, but closer to $\propto -F$ at lower AR. The optical transition strength elucidates this behavior, encapsulating that the zero-field $e1$-$h1$ overlap decreases at lower AR. As the QD becomes narrower and taller the $e1$ and $h1$ wave functions become more offset along [001], which reduces their overlap and hence the band edge absorption. We note a marked reduction of the $e1$-$h1$ optical transition strength for AR < 4:1. These trends are borne out in Fig. 4(c), which shows the absorption spectra vs. F for AR = 3:1 (left) and 5:1 (right). We note reduced zero-field absorption in the 3:1 AR QD. Further analysis reveals that the zero-field absorption

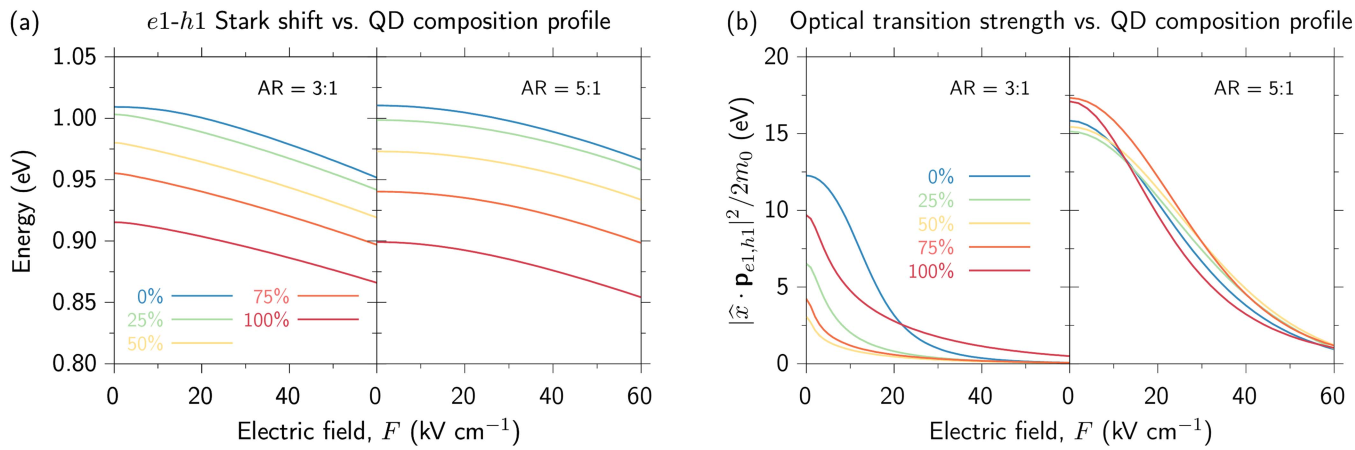

Fig. 5. (a) Stark shift, and (b) Kane energy (optical transition strength) of the $e1$-$h1$ band gap vs. [100] lateral applied electric field strength F for square-base truncated pyramidal QDs having AR $= 3{:}1$ (left panels) and 5:1 (right panels). Each QD is alloyed $In_xGa_{1-x}As$ at its base, with the In composition x increasing linearly with distance along [001] to reach pure InAs ($x = 1$) at the QD's apex. Starting from a pure InAs QD having $x = 1$ ($= 100\%$, red) throughout, the base In composition is reduced to $x = 0$ ($= 0\%$, blue).

edge in the 3:1 AR QD is not dominated by the weak $e1$-$h1$ transition, but consists primarily of contributions from bound state transitions at higher energy. These contributions reduce the rate at which the absorption edge shifts vs. F compared to the $e1$-$h1$ band gap shown in Fig. 4(a) for AR $= 3{:}1$. Applying a lateral field further reduces the $e1$-$h1$ overlap. In the 3:1 AR QD this produces low absorption close to 1.3 μm, contrary to what is required for an EAM. This contrasts with the 5:1 AR QD, for which we observe a robust lateral-field QCSE with appreciable absorption close to 1.3 μm for $F \approx 45$ kV cm^{-1}.

Finally, we consider the impact of the vertical In composition profile. Considering a graded In composition along [001] captures the experimentally inferred inverted $e1$-$h1$ alignment, but it is uncertain how the base and apex In compositions should be chosen, or what the functional form of the composition profile should be. Based on Ref. [37] we considered a linear In composition profile, with the In composition increasing from $x = 0.5$ at the base to $x = 1$ at the apex. We now quantify the impact of varying the base In composition, while keeping the apex fixed as pure InAs. Fig. 5(a) and (b) respectively show the $e1$-$h1$ Stark shift and optical transition strength vs. [100] F for QDs having AR $= 3{:}1$ (left panels) and 5:1 (right panels), as the In composition at the base is increased from $x = 0$ (GaAs; blue) to $x = 1$ (InAs; red). For higher AR $= 5{:}1$ the primary effect of changing the vertical composition profile is to decrease the $e1$-$h1$ band gap as the base In composition is increased. However, the impact on the optical transition strength, and the overall lateral QCSE, is otherwise minimal. For lower AR $= 3{:}1$ we note a marked decrease in $e1$-$h1$ optical transition strength, due to the aforementioned vertical offset between $e1$ and $h1$. As the QD base is changed from GaAs to InAs, $h1$ shifts from being localized close to the QD apex to being localized towards the base. This causes $|\psi_{h1}(\mathbf{r})|^2$ to expand in-plane as the lateral extent of the QD increases towards the QD base. This can impede $h1$ from contributing to the absorption and, as described above, can result in dominant contributions involving higher-energy transitions. At low AR the $e1$-$h1$ optical transition strength is maximized when the QD base is In-free. Taken together with the above AR analysis, these results emphasize the importance of the vertical $e1$-$h1$ offset in determining the electroabsorption characteristics. We conclude that QDs having AR $\gtrsim 4{:}1$ are best suited to lateral-field EAM applications, to mitigate the deleterious impact of a large vertical $e1$-$h1$ offset on the magnitude of the band edge absorption. Transmission and tunneling microscopy imaging studies have shown self-assembled $In_xGa_{1-x}As/GaAs$ QDs to reliably admit ARs $\sim 3{:}1$ [8], [18], [44]. It has, however, also been demonstrated that the AR can be increased by varying the growth deposition rate, with ARs $\sim 5{:}1$ having been observed [45], [46], [47].

IV. Implications for Devices

The above analysis highlights that the lateral-field QCSE can display strong sensitivity to the morphology and absorption edge FWHM in 1.3 μm $In_xGa_{1-x}As/GaAs$ QDs. We have identified two aspects as paramount to enable operation of datacom-wavelength lateral QD-EAMs: (i) high base-to-height AR, to deliver high absorption by maximizing the zero-field $e1$-$h1$ overlap, and (ii) low absorption edge FWHM, to realize high extinction ratio at the modulation wavelength.

From the perspective of epitaxial growth, realizing viable QD-EAMs poses a series of interconnected challenges. First, the requirement for low absorption edge FWHM mandates high QD uniformity in a given sample. Second, high uniformity must be realized for QDs having ARs $\gtrsim 4{:}1$. Third, any In composition gradients in the QDs must not compromise the ground state $e1$-$h1$ overlap, so high optical absorption can be retained at the desired modulation wavelength and voltage. We note, however, that these challenges are broadly common to those associated with the development of III-V on Si QD lasers, where consistent refinements have delivered high-performance devices. Exerting control over QD morphology while maintaining high uniformity is challenging, but a degree of such control can be realized through careful selection of growth temperature and deposition rate. Approaches to promote QD uniformity have allowed the realization of samples with low FWHM < 17 meV [38], [39]. While typical FWHMs are closer to 30 meV, our analysis in Section III-B demonstrates that the associated degradation of QD-EAM performance can be mitigated by targeting QDs in which the zero-field band gap possesses a larger blueshift with respect to the target modulation wavelength. Finally, while it is known that a varying composition profile along [001] is required to account for the observed nature of the vertical QCSE [36], [37], little is known about the potential impact of lateral compositional inhomogeneities. Recent analysis [48] considered the impact of lateral compositional variations on the QD electronic properties, finding their impact to be minimal. Nevertheless, lateral variations in composition profile can potentially impact the lateral QCSE. Given the current lack of information regarding lateral composition profiles, we assert that such effects are best investigated in the context of theory-experiment comparisons for specific samples.

From the perspectives of device fabrication and operation, additional minor considerations are evident. First, designing lateral electrical contacts should account for the potential sensitivity of the lateral-field QCSE to the in-plane orientation of the applied electric field. Our analysis suggests that EAM performance could potentially suffer minor degradation if the field is applied along [$\bar{1}$10], but that this is only expected to be a possibility for circular-base QDs. Second, the lateral QCSE can also be impacted by variations in QD morphology within a given sample. At zero-field, local changes in $e1$-$h1$ band gap associated with variable QD morphology increase the absorption edge FWHM. Recalling the perturbation theoretic result $\Delta E \propto -m^* a^4 F^2$ we note that the Stark shift depends on extent ($\sim a$) of a given QD. At non-zero field the $e1$-$h1$ band gap thus shifts at different rates vs. F in differently-sized QDs, acting to increase the FWHM with increasing F for a real QD array. Since this effect is not explicitly captured by our single-QD calculations, test calculations were undertaken for a series of QDs whose dimensions vary by $\pm 5\%$. These calculations suggest that the additional contribution to the field-dependent FWHM $\Delta(F)$ due to variations in QD size is minimal across the range of F investigated herein. However, if pronounced, we note that this effect can potentially benefit EAM operation: increasing $\Delta(F)$ with increasing F produces a larger redshift of the absorption edge at fixed F, such that the modulation voltage could potentially be reduced while retaining high α_F/α_0.

Despite these challenges, our results indicate that 1.3 μm $In_xGa_{1-x}As$/GaAs QDs offer significant potential to develop monolithically integrated QD-EAMs for high-speed datacoms applications. Utilizing QDs to develop lateral EAMs has the potential to deliver clear benefits for practical applications. First, the three-dimensional carrier confinement in a QD allows the realization of a strong lateral-field QCSE. For example, the magnitude of the lateral-field Stark shift at fixed F predicted here is approximately twice as large as the already "strong" vertical QCSE in Ge/Si_xGe_{1-x}/Si QW-EAMs [49]. This suggests the possibility to develop lateral QD-EAMs demonstrating high extinction ratios as in the incumbent InP-based vertical QW-EAM technology. However, it is important to note that in a conventional vertical QW-EAM the modulation voltage is dropped across a typical intrinsic region thickness ~ 0.5 μm. Lateral electrical contacting on either side of a waveguide may result in having to drop the modulation voltage over a typical waveguide thickness $\sim$ 1 - 2 μm in a lateral QD-EAM. It may then be the case that a larger modulation voltage is required to produce a given electric field F within the QD active region. Second, a lateral-field QD-EAM is expected to operate at higher bandwidth than its vertical counterpart. The bandwidth of a conventional vertical EAM is limited by the device (junction) and signal pad (parasitic) capacitance. However, a lateral EAM is expected to admit lower junction capacitance due to the increased junction length, and to mitigate parasitic capacitance since the contacts are coupled electrically only via the device [21]. This mirrors the design employed in Si-based EAMs and Mach-Zehnder modulators which have demonstrated high modulation bandwidths [50], [51], [52], but with reduced modulation efficiency – quantified by the ratio of extinction ratio and insertion loss – compared to InP-based III-V QW-EAMs [53], [54], [55]. Third, sustained efforts to enhance the performance of III-V on Si QD lasers have produced a viable platform upon which integrated QD-EAM operation can be demonstrated.

V. Conclusion

We have demonstrated the viability of lateral-field EAMs utilizing 1.3 μm $In_xGa_{1-x}As$/GaAs QDs for integration in high-speed Si photonic integrated circuits. Comparing application of a lateral electric field to the conventional vertical orientation revealed a robust lateral-field QCSE, allowing to tune the optical absorption edge close to 1.3 μm at electric fields compatible with EAM device operation. This comparison highlighted that the lateral-field Stark shift significantly exceeds its vertical-field counterpart at fixed field strength, due to the large base-to-height AR that characterizes self-assembled $In_xGa_{1-x}As$/GaAs QDs. Detailed calculations quantified the sensitivity of the lateral-field QCSE to both the QD morphology and the in-plane orientation of the applied electric field. Experimental analysis of the conventional vertical-field QCSE has revealed "inverted" electron-hole alignment – whereby the ground state hole wave function localizes above the ground state electron wave function along [001] – which can be captured in theoretical calculations by including an In composition gradient along [001]. For AR $\lesssim$ 4:1 we found that the presence of a vertical In composition gradient can significantly reduce a QD's ground state optical transition strength, but that its impact is effectively mitigated for ARs $\gtrsim$ 4:1. Our systematic analysis of the impact of QD morphology on the lateral-field QCSE highlights that QDs having large ARs $\gtrsim$ 5:1 are best suited to optimize EAM operation, with enhanced performance expected for QDs that demonstrate low absorption edge linewidth (Gaussian FWHM $\Delta \lesssim 25$ meV). Overall, our results suggest the possibility to leverage recent advances in the development and fabrication of III-V on Si QD lasers and single-photon sources to realize monolithically integrated high-speed lateral-field QD-EAMs, to significantly enhance the functionality of nascent III-V on Si integrated photonics.

Acknowledgment

The authors thank Drs. Xing Dai and Mateusz Piekarek (Tyndall National Institute, Ireland) for useful discussions.

References

[1] S. L. Chuang, *Physics of Photonic Devices*, 2nd ed. Hoboken, NJ, USA: Wiley, 2009.
[2] K. W. Böer, H. J. Hänsch, and U. Kümmel, "Anwendung elektrooptischer Effekte zur Analyse des elektrischen Leitungsvorganges in CdS-Einkristallen," *Zeitschrift fur Physik*, vol. 155, 1959, Art. no. 170.
[3] D. A. B. Miller, D. S. Chemla, and S. Schmitt-Rink, "Relation between electroabsorption in bulk semiconductors and in quantum wells: The quantum-confined Franz-Keldysh effect," *Phys. Rev. B*, vol. 33, 1986, Art. no. 6976.
[4] D. A. B. Miller et al., "Band-edge electroabsorption in quantum well structures: The quantum-confined Stark effect," *Phys. Rev. Lett.*, vol. 53, 1984, Art. no. 2173.
[5] J. E. Cunningham, "Recent developments and applications in electroabsorption semiconductor modulators," *Mater. Sci. Eng.: R: Rep.*, vol. 25, pp. 155–194, 1999.
[6] P. Dong, Y. Chen, G. Duan, and D. T. Neilson, "Silicon photonic devices and integrated circuits," *Nanophotonics*, vol. 3, pp. 215–228, 2014.
[7] T. Wang, H. Liu, A. Lee, F. Pozzi, and A. Seeds, "1.3-μm InAs/GaAs quantum-dot lasers monolithically grown on Si substrates," *Opt. Exp.*, vol. 19, no. 12, 2011, Art. no. 11381.
[8] S. Chen et al., "Electrically pumped continuous-wave III–V quantum dot lasers on silicon," *Nat. Photon.*, vol. 10, pp 307–311, 2016.
[9] A. Y. Liu et al., "Electrically pumped continuous-wave 1.3 μm quantum-dot lasers epitaxially grown on on-axis (001) GaP/Si," *Opt. Lett.*, vol. 42, no. 2, pp. 338–341, 2017.
[10] S. Chen et al., "Electrically pumped continuous-wave 1.3 μm InAs/GaAs quantum dot lasers monolithically grown on on-axis Si (001) substrates," *Opt. Exp.*, vol. 25, 2017, Art. no. 4632.
[11] Y. Wang et al., "InAs/GaAs quantum-dot lasers grown on on-axis Si (001) without dislocation filter layers," *Opt. Exp.*, vol. 31, pp. 4862–4872, 2023.
[12] J. C. Norman, D. Jung, Y. Wan, and J. E. Bowers, "Perspective: The future of quantum dot photonic integrated circuits," *APL Photon.*, vol. 3, 2018, Art. no. 030901.
[13] D. Liang and J. E. Bowers, "Recent progress in heterogeneous III-V-on-Silicon photonic integration," *Light: Adv. Manuf.*, vol. 2, no. 5, pp. 59–83, 2021.
[14] V. Cao et al., "Recent progress of quantum dot lasers monolithically integrated on Si platform," *Front. Phys.*, vol. 10, 2022, Art. no. 839953.
[15] Z. Xiao et al., "Recent progress in silicon-based photonic integrated circuits and emerging applications," *Adv. Opt. Mater.*, vol. 11, no. 20, 2023, Art. no. 2301028.
[16] J. Selvidge et al., "Reduced dislocation growth leads to long lifetime InAs quantum dot lasers on silicon at high temperatures," *Appl. Phys. Lett.*, vol. 118, 2021, Art. no. 192101.
[17] C. Shang et al., "Electrically pumped quantum-dot lasers grown on 300 mm patterned Si photonic wafers," *Light: Sci. Appl.*, vol. 11, 2022, Art. no. 299.
[18] K. Papatryfonos et al., "Low-defect quantum dot lasers directly grown on silicon exhibiting low threshold current and high output power at elevated temperatures," *Adv. Photon. Res.*, vol. 6, 2024, Art. no. 2400082.
[19] H. Deng et al., "1.3 μm InAs/GaAs quantum-dot lasers with p-type, n-type, and co-doped modulation," *Adv. Photon. Res.*, vol. 3, 2024, Art. no. 2400045.
[20] A. W. Elshaari, W. Pernice, K. Srinivasan, O. Benson, and V. Zwiller, "Hybrid integrated quantum photonic circuits," *Nat. Photon.*, vol. 14, no. 5, 2020, Art. no. 285.
[21] K. Hasebe et al., "High-speed modulation of lateral p-i-n diode structure electro-absorption modulator integrated with DFB laser," *J. Lightw. Technol.*, vol. 33, pp. 1235–1240, Mar. 2015.
[22] T. B. Bahder, "Eight-band $\mathbf{k}\cdot\mathbf{p}$ model of strained zinc-blende crystals," *Phys. Rev. B*, vol. 41, 1990, Art. no. 11992.
[23] A. M. Cohen and G. E. Marques, "Electronic structure of zinc-blende-structure semiconductor heterostructures," *Phys. Rev. B*, vol. 41, 1990, Art. no. 10608.
[24] E. P. O'Reilly, O. Marquardt, S. Schulz, and A. D. Andreev, "Chapter 5: Plane-wave approaches to the electronic structure of semiconductor nanostructures," in *Multi-Band Effective Mass Approximations*. Berlin, Germany: Springer, 2014.
[25] S. Tomić, A. G. Sunderland, and I. J. Bush, "Parallel multi-band $\mathbf{k}\cdot\mathbf{p}$ code for electronic structure of zinc blend semiconductor quantum dots," *J. Mater. Chem.*, vol. 16, 2006, Art. no. 1963.
[26] A. D. Andreev, J. R. Downes, D. A. Faux, and E. P. O'Reilly, "Strain distributions in quantum dots of arbitrary shape," *J. Appl. Phys.*, vol. 86, pp. 297–305, 1999.
[27] A. Schliwa, M. Winkelnkemper, and D. Bimberg, "Impact of size, shape, and composition on piezoelectric effects and electronic properties of In(Ga)As/GaAs quantum dots," *Phys. Rev. B*, vol. 76, 2007, Art. no. 205324.
[28] I. Vurgaftman and J. R. Meyer, "Band parameters for III–V compound semiconductors and their alloys," *J. Appl. Phys.*, vol. 89, pp. 5815–5875, 2001.
[29] M. A. Caro, S. Schulz, and E. P. O'Reilly, "Origin of nonlinear piezoelectricity in III-V semiconductors: Internal strain and bond ionicity from hybrid-functional density functional theory," *Phys. Rev. B*, vol. 91, 2015, Art. no. 075203.
[30] N. Vukmirović and S. Tomić, "Plane wave methodology for single quantum dot electronic structure calculations," *J. Appl. Phys.*, vol. 103, 2008, Art. no. 103718.
[31] F. Smulowicz, "Derivation of a general expression for the momentum matrix elements within the envelope-function approximation," *Phys. Rev. B*, vol. 51, 1995, Art. no. 1613.
[32] C. Murphy, E. P. O'Reilly, and C. A. Broderick, "Theory and optimisation of radiative recombination in broken-gap InAs/GaSb superlattices," *J. Phys. D: Appl. Phys.*, vol. 57, 2024, Art. no. 035103.
[33] N. Liu, J. Tersoff, O. Baklenov, A. L. Holmes, and C. K. Shih, "Nonuniform composition profile in $In_{0.5}Ga_{0.5}As$ alloy quantum dots," *Phys. Rev. Lett.*, vol. 84, 2000, Art. no. 334.
[34] D. M. Bruls et al., "Determination of the shape and indium distribution of low-growth-rate InAs quantum dots by cross-sectional scanning tunneling microscopy," *Appl. Phys. Lett.*, vol. 81, 2002, Art. no. 1708.
[35] J. Stangl, V. Holý, and G. Bauer, "Structural properties of self-organized semiconductor nanostructures," *Rev. Mod. Phys.*, vol. 76, 2004, Art. no. 725.
[36] P. W. Fry et al., "Inverted electron-hole alignment in InAs/GaAs self-assembled quantum dots," *Phys. Rev. Lett.*, vol. 84, 2000, Art. no. 733.
[37] J. A. Barker and E. P. O'Reilly, "Theoretical analysis of electron-hole alignment in InAs-GaAs quantum dots," *Phys. Rev. B*, vol. 61, 2000, Art. no. 13840.
[38] K. Y. K. Yamaguchi, K. Y. K. Yujobo, and T. K. T. Kaizu, "Stranski-Krastanov growth of InAs quantum dots with narrow size distribution," *Jpn. J. Appl. Phys.*, vol. 39, 2000, Art. no. L1245.
[39] T. Yang, J. Tatebayashi, S. Tsukamoto, M. Nishioka, and Y. Arakawa, "Narrow photoluminescence linewidth ($<$17 meV) from highly uniform self-assembled InAs/GaAs quantum dots grown by low-pressure metalorganic chemical vapor deposition," *Appl. Phys. Lett.*, vol. 84, 2004, Art. no. 2817.
[40] M. K. Chin, "On the figures of merit for electroabsorption waveguide modulators," *IEEE Photon. Tech. Lett.*, vol. 4, no. 7, pp. 726–728, Jul. 1992.
[41] M. K. Chin and W. S. C. Chang, "Electroabsorption properties of InGaAs/InAlAs multiple quantum well structures at 1.5 μm," *IEEE Photon. Tech. Lett.*, vol. 6, no. 4, pp. 502–504, Apr. 1994.
[42] J. Kwoen et al., "All MBE grown InAs/GaAs quantum dot lasers on on-axis Si (001)," *Opt. Exp.*, vol. 26, no. 9, pp. 11568–11576, 2018.
[43] T. Kageyama et al., "Extremely high temperature (220 °C) continuous-wave operation of 1300-nm-range quantum-dot lasers," in *Proc 2011 Conf. Lasers Electro- Opt. Europe 12th Eur. Quantum Electron. Conf.*, 2011, pp. 1–1.
[44] A. Lenz et al., "Structure of InAs quantum dots-in-a-well nanostructures," *Physica E*, vol. 40, 2008, Art. no. 1988.
[45] P. Kratzer et al., "Shape transition during epitaxial growth of InAs quantum dots on GaAs(001): Theory and experiment," *Phys. Rev. B*, vol. 73, 2006, Art. no. 205347.
[46] S. Tsukamoto, T. Honma, G. R. Bell, A. Ishii, and Y. Arakawa, "Atomistic insights for InAs quantum dot formation on GaAs(001) using STM within a MBE growth chamber," *Small*, vol. 2, no. 3, pp. 386–389, 2006.
[47] R. Murray et al., "1.3 µm room temperature emission from InAs/GaAs self-assembled quantum dots," *Japanese J. Appl. Phys.*, vol. 38, no. 1S, 1999, Art. no. 528.
[48] A. N. Kosarev, V. V. Chaldyshev, and N. Cherkashin, "Experimentally-verified modeling of InGaAs quantum dots," *Nanomaterials*, vol. 12, 2022, Art. no. 1967.

[49] Y.-H. Kuo et al., “Strong quantum-confined Stark effect in germanium quantum-well structures on silicon,” *Nature*, vol. 437, 2005, Art. no. 1334.
[50] L. Mastronardi et al., “High-speed Si/GeSi hetero-structure electro absorption modulator,” *Opt. Exp.*, vol. 26, 2018, Art. no. 6663.
[51] J. Fujikata et al., “High-performance Ge/Si electro-absorption optical modulator up to 85 °C and its highly efficient photodetector operation,” *Opt. Exp.*, vol. 31, no. 6, 2023, Art. no. 10732.
[52] L. Yang and J. Ding, “High-speed silicon Mach–Zehnder optical modulator with large optical bandwidth,” *J. Light. Technol.*, vol. 32, pp. 966–970, 2014.
[53] W. Kobayashi et al., “Design and fabrication of 10-/40-Gb/s, uncooled electroabsorption modulator integrated DFB laser with butt-joint structure,” *J. Lightw. Technol.*, vol. 28, no. 1, pp. 164–171, 2010.
[54] M. Baier et al., “Integrated transmitter devices on InP exploiting electro-absorption modulation,” *PhotoniX*, vol. 1, pp. 1–11, 2020.
[55] S. Lee, N. Kim, M. Park, and O.-K. Kwon, “1.3 μm identical active electro-absorption modulated laser with quantum well intermixed passive waveguide,” *Opt. Exp.*, vol. 32, no. 3, pp. 3278–3289, 2024.

Tommy Murphy was born in Cork, Ireland. He received the B.Sc. (Hons.) degree in physics from University College Cork, Cork, Ireland, in 2019. In 2021, he received the M.Sc. degree from University College Cork, where he worked on the theoretical analysis of light propagation through curved optical waveguides in the Integrated Photonics Group, Tyndall National Institute, Cork, Ireland. He is currently a Ph.D. student in the Photonics Theory Group, Tyndall National Institute. He works on the theoretical analysis of components for photonic integrated circuits.

Christopher A. Broderick was born in London, U.K. He received the B.Sc. (Hons.) and Ph.D. degrees in physics from University College Cork, Ireland in 2010 and 2015, respectively. From 2015 to 2016 he was a Postdoctoral Research Associate with the Photonics and Quantum Group, University of Bristol, Bristol, U.K. From 2017 to 2021 he was a Postdoctoral Researcher with the Photonics Theory Group, Tyndall National Institute, Cork, Ireland, where from 2018 to 2020 he was the National University of Ireland Postdoctoral Fellow in the Sciences. Since 2021 he has been a Staff Researcher with Tyndall National Institute, and from 2022 to 2023 he was seconded to the Materials Department at the University of California, Santa Barbara, USA as a Marie Skłodowska-Curie Individual (Global) Fellow. He is currently a Royal Society-Research Ireland University Research Fellow with the School of Physics, University College Cork. He has authored more than 50 journal and conference papers relating to the theory of the electronic, optical and transport properties of emerging semiconductor material systems, and the simulation and design of novel heterostructure concepts for photonics applications.

Frank H. Peters was born in Victoria, Canada. He received the B.Eng. degree in engineering physics from the Technical University of Nova Scotia, Canada, in 1988, and the Ph.D. degree from McMaster University, Hamilton, Canada, in 1991. From 1991 to 1993, he was a Research Engineer with the Electrical and Computer Engineering Department, University of California, Santa Barbara, USA. From 1993 to 2001, he was a Research Scientist with Optical Concepts, W. L. Gore and Associates, and Agilent Technologies, developing integrated photonic devices for datacom and telecom applications. From 2001 to 2005, he was with Infinera, Sunnyvale, USA, where he was involved in the development of high-speed photonic integrated circuits, and then moved to Ireland in 2005. He is currently a Professor with the School of Physics, University College Cork, Cork, Ireland, and is also Head of the Integrated Photonics Group, Tyndall National Institute, Cork. He has authored more than 240 journal and conference papers and holds more than 40 patents, concerned with thermal, optical, electrical and systems’ issues relating to the design and use of photonic devices and high-speed photonic integrated circuits.

Eoin P. O’Reilly was born in Dublin, Ireland. He received the B.A. degree in theoretical physics from Trinity College Dublin, Ireland, in 1978, and the Ph.D. degree in theoretical condensed matter physics from the University of Cambridge, U.K. in 1982. From 1984 to 2001 he was with the University of Surrey, Guildford, U.K., where he was the Head of the Department of Physics from 1997 to 2001. Since 2001, he has been with Tyndall National Institute, Ireland, where he was founding Head of the Photonics Theory Group, and a Research Professor with the School of Physics, University College Cork, Ireland. From 2014 to 2022, he served as Chief Scientist at Tyndall National Institute, and from 2017 to 2018 was Interim CEO. His research interests include developing the fundamental understanding of photonic materials and devices, to enable the design of structures for new capabilities and applications. In 2014, he was a co-recipient of the Rank Prize for Optoelectronics, in recognition of his pioneering work on strained-layer semiconductor lasers.